



Cite this: *RSC Adv.*, 2024, **14**, 29083

## Fabrication of rare-earth cerium-doped nickel–copper ferrite as a promising photo-catalyst for congo red-containing wastewater treatment

Morsheda Akhter, Md. Khairul Amin, Palash Kumar Dhar, Shishir Kumar Dey, Muhammad Sarwar Hossain  and Sagar Kumar Dutta \*

Synthetic organic dyes are becoming the major class of water pollutants leading to malignant detriments to the ecology. Consequently, this research focuses on remediating this circumstance utilizing a novel catalytic material, namely, cerium-doped spinel ferrite  $\text{Ni}_{0.6}\text{Cu}_{0.4}\text{Ce}_x\text{Fe}_{2-x}\text{O}_4$  ( $x = 0.0, 0.5, 1.0, 1.5$ ), developed using the chemical coprecipitation technique and characterized using FTIR, XRD, FE-SEM, EDX and VSM analysis. The particles have shown band gap values ranging from 4.29 to 2.01 eV. The as-synthesized nano-sized particles were employed as a photocatalyst to degrade the complex structure of congo red (CR) dye. About 91% of the dye was degraded with 60 mg of the catalyst under visible light irradiation with the highest cerium-doping ( $x = 1.5$ ) at a pH below 6.8, which was the zero-surface charge pH for the particle. Batch studies were performed to optimize all the conditions, including the dose, concentration, pH, and different light energy sources. Recyclability of the catalyst was also investigated, which was supported by the higher stability of the recovered particles through XRD analysis. Reaction kinetics for this system were evaluated along with three isotherm models. Moreover, the scavenging test indicated that the major active species leading to this degradation was hole ( $\text{h}^+$ ), and a schematic degradation mechanism is presented. Following that, this model can successfully be used for wastewater treatment.

Received 13th June 2024  
 Accepted 1st September 2024

DOI: 10.1039/d4ra04334k  
[rsc.li/rsc-advances](http://rsc.li/rsc-advances)

### 1. Introduction

Heterogeneous photocatalysis serves as an adaptable treatment approach for an extensive array of pollutants in water. Nanomaterials are popular as heterogeneous catalysts for the degradation of organic dyes, which are one of the major classes of organic pollutants in water sources.<sup>1</sup> These nanomaterials possess a considerably high surface area, making them exceptionally efficient for photocatalysis, and they are economical in terms of catalyst recovery after treatment.<sup>2</sup> The oxidative degradation of large organic dye molecules, commonly referred to as advanced oxidation processes (AOPs), utilizes heterogeneous nano-catalysts to produce smaller molecules (such as  $\text{CO}_2$ ,  $\text{H}_2\text{O}$ , etc.) with the assistance of external light energy. This protocol presents a promising and fascinating approach to wastewater treatment in contemporary times.<sup>3</sup> AOP with photocatalysts works through the process of electronic transition from the valence band to the conduction band, leading to the generation of electron–hole ( $\text{e}^-/\text{h}^+$ ) pairs on the catalyst surface, which actively participate in the degradation of organic compounds.<sup>4</sup>

*Chemistry Discipline, Khulna University, Khulna 9208, Bangladesh. E-mail: [sagar@chem.ku.ac.bd](mailto:sagar@chem.ku.ac.bd) [khairul.che@ku.ac.bd](mailto:khairul.che@ku.ac.bd)*

Azo dyes are considered as both the oldest class and largest type of synthetic dyes, owing to their compatibility for various substrate materials. Congo red (CR) is a diazo dye that is widely used in textile industries owing to its greater adherence for cellulose fibers. It is also used in the diagnosis of amyloidosis and as a pH indicator.<sup>5</sup> It has been proven to be carcinogenic to humans, even at low concentrations, impairing aquatic system homeostasis. Its short-term effects in humans include diarrhea, vomiting, and nausea, while long-term exposure can lead to mutagenic and genotoxic effects.<sup>6</sup> Various approaches have been adopted for the removal of CR from wastewater, including adsorption, biological treatment, physicochemical treatment, coagulation/flocculation, ozonation, photocatalytic degradation, biodegradation, and catalytic reduction.<sup>7</sup> Among them, photocatalysis using nanomaterials has attained greater acceptance due to its excellent degradation efficiency, easy and convenient methods, and production of non-toxic metabolites after degradation.<sup>8,9</sup>

Spinel ferrite is a class of composite material that is gaining special attention because of its prominent features, including its application as a magnetic material in devices, such as recording disks, electrical motors, microphones, and sensors.<sup>10,11</sup> Ferrites can exist in the form of a single-phase spinel ( $\text{AFe}_2\text{O}_4$ ) or doped spinel  $[(\text{A}_x\text{B}_y)\text{Fe}_2\text{O}_4]$ , and the spinel structure can even be doped with various rare earth ions to alter



the lattice's physical characteristics. Moreover, spinel ferrites fabricated with nickel and copper ions have demonstrated their excellent physicochemical properties.<sup>12,13</sup> Rare-earth cerium, in its simple oxide form, exhibits very effective catalytic performance. However, it is challenging to insert the cerium ion ( $\text{Ce}^{3+}$ ) with its larger ionic radius into the crystal structure of ferrite by replacing  $\text{Fe}^{3+}$  ions, which have a comparatively smaller ionic radius.<sup>14</sup> Nevertheless, the successful insertion of  $\text{Ce}^{3+}$  can impart excellent properties, such as reduced crystallite size because of its hindrance to crystal growth. Moreover,  $\text{Ce}^{3+}$  tends to the octahedral voids of the spinel ferrite lattice.<sup>15</sup> This octahedral site occupancy, along with the smaller crystallite size and high surface-to-volume ratio, can significantly enhance the catalytic performance of the ferrite, as the octahedral sites are the catalytically active parts.<sup>16</sup> The synthesis methods play an important role in producing high-quality ferrite materials in terms of morphology, purity, stability, and surface area. Currently, various synthesis methods are used for the preparation of ferrite materials, such as chemical co-precipitation,<sup>17</sup> hydrothermal,<sup>18</sup> and sol-gel,<sup>19</sup> each of which has its own advantages and disadvantages. The chemical coprecipitation method is particularly attractive owing to its simplicity, shorter reaction time, lower cost, mild reaction conditions, and high activity.<sup>20,21</sup>

Few works have been reported with cerium-doping in spinel ferrite for use as a photocatalyst to degrade organic dye. Following that, this research aims to develop a spinel ferrite catalyst by incorporating rare-earth  $\text{Ce}^{3+}$  ion,  $\text{Ni}_{0.6}\text{Cu}_{0.4}\text{Ce}_x\text{Fe}_{2-x}\text{O}_4$  ( $x = 0.0, 0.5, 1.0, 1.5$ ) using the chemical co-precipitation method. Analytical methods, including FT-IR, XRD, FE-SEM, EDX, and VSM, were used to evaluate the successful fabrication of the material, which was studied as an exemplar framework catalyst for the photo-degradation of organic congo red (CR) dye in aqueous solutions. Along with different parameters, such as pH, concentration of the dye solution, dose of the catalyst, and different light sources, the mechanism of this degradation process was investigated using the scavenging test.

## 2. Experimental

### 2.1. Materials

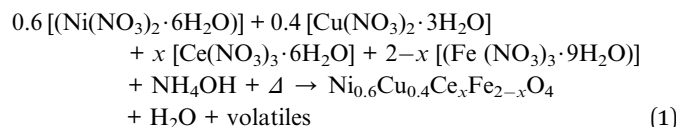
Analytical grade reagents (purity 99%), including cerium nitrate hexahydrate ( $\text{Ce}(\text{NO}_3)_3 \cdot 6\text{H}_2\text{O}$ ), nickel nitrate hexahydrate ( $\text{Ni}(\text{NO}_3)_2 \cdot 6\text{H}_2\text{O}$ ), copper nitrate trihydrate ( $\text{Cu}(\text{NO}_3)_2 \cdot 3\text{H}_2\text{O}$ ), ferric nitrate nonahydrate ( $\text{Fe}(\text{NO}_3)_3 \cdot 9\text{H}_2\text{O}$ ), ammonia solution ( $\text{NH}_4\text{OH}$ ), ethanol ( $\text{C}_2\text{H}_5\text{OH}$ ), congo red ( $\text{C}_{32}\text{H}_{22}\text{N}_6\text{Na}_2\text{O}_6\text{S}_2$ ), sodium chloride ( $\text{NaCl}$ ), disodium EDTA ( $\text{C}_{10}\text{H}_{16}\text{N}_2\text{Na}_2\text{O}_8$ ), isopropyl alcohol ( $\text{C}_3\text{H}_8\text{O}$ ), and potassium dichromate ( $\text{K}_2\text{Cr}_2\text{O}_7$ ) were purchased from Merck, India, and used without any further purification. Deionized water (WGH201 ion exchange) was used throughout the experiment.

### 2.2. Synthesis of $\text{Ni}_{0.6}\text{Cu}_{0.4}\text{Ce}_x\text{Fe}_{2-x}\text{O}_4$

The synthesis of  $\text{Ni}_{0.6}\text{Cu}_{0.4}\text{Ce}_x\text{Fe}_{2-x}\text{O}_4$  ( $x = 0.0, 0.5, 1.0, 1.5$ ) was performed using the co-precipitation method, as described in

the literature,<sup>22–25</sup> and is schematically represented in Fig. 1. Stoichiometric amounts of  $\text{Ni}(\text{NO}_3)_2 \cdot 6\text{H}_2\text{O}$ ,  $\text{Cu}(\text{NO}_3)_2 \cdot 3\text{H}_2\text{O}$ ,  $\text{Ce}(\text{NO}_3)_3 \cdot 6\text{H}_2\text{O}$ , and  $\text{Fe}(\text{NO}_3)_3 \cdot 9\text{H}_2\text{O}$  were dissolved in 50 mL of water. The solutions were then mixed together and stirred overnight using a magnetic stirrer. Afterward, 25% of  $\text{NH}_3$  solution was added dropwise to the mixture as a precipitating agent at 60 °C, initiating particle formation. The pH of the mixture was adjusted to about 10. The mixture was then kept under stirring at 60 °C for 1 h to complete the reaction. The resulting precipitate was left overnight, and then washed several times with water and ethanol to adjust the pH to near 7. The particles were subsequently dried in an oven at 100 °C, and finally calcined in a muffle furnace at 700 °C for 4.5 h.

The reactions that take place during the process can be represented as follows:



### 2.3. Characterization

The formation of metal–oxygen bonds within the crystal lattice of the ferrite samples was analyzed using Fourier transform infrared (FT-IR) spectroscopy within the range of 300–4000  $\text{cm}^{-1}$  using the SHIMADZU IR Spirit Fourier transform infrared spectrometer. X-ray diffraction (XRD) measurements were conducted at the Material Science Division of Atomic Energy Center, Dhaka, Bangladesh, using a Philips X'pert PRO X-ray diffractometer with  $\text{CuK}_\alpha$  radiation (1.5418 Å) to confirm the phase formation of the crystal. Surface morphology and elemental analysis were performed using field-emission scanning electron microscopy (FE-SEM) and energy dispersive X-ray (EDX) spectroscopy (JEOL JSM-7600F). The magnetic properties of the samples were analyzed using a Microsense vibrating sample magnetometer (VSM) model EV7 at the Atomic Energy Center, Dhaka, Bangladesh. The point of zero charge (pH<sub>PZC</sub>) study was performed using the pH drift method, as reported previously with slight modifications.<sup>26</sup>

### 2.4. Photocatalytic degradability test

In this study, the photocatalytic degradation process of CR was analyzed using the synthesized  $\text{Ni}_{0.6}\text{Cu}_{0.4}\text{Ce}_x\text{Fe}_{2-x}\text{O}_4$  material. In an optimized case, 50 mL of a 40 ppm CR dye solution was stirred with 60 mg of catalyst for 10 min in a dark system to obtain the adsorption–desorption equilibrium between the catalyst surface and dye molecules. Subsequently, the mixture was irradiated with a light energy source. At intervals of 10 min, aliquots of the sample solution were taken, and particles were separated by centrifugation. The absorbance of the solution was measured using a UV-visible spectrophotometer (SHIMADZU UV-1900i). CR dye exhibits absorbance maxima at a wavelength ( $\lambda_{\text{max}}$ ) of 498 nm. At each time point, the absorbance value at 498 nm was recorded, and the remaining concentration of the CR solution was calculated using the calibration curve



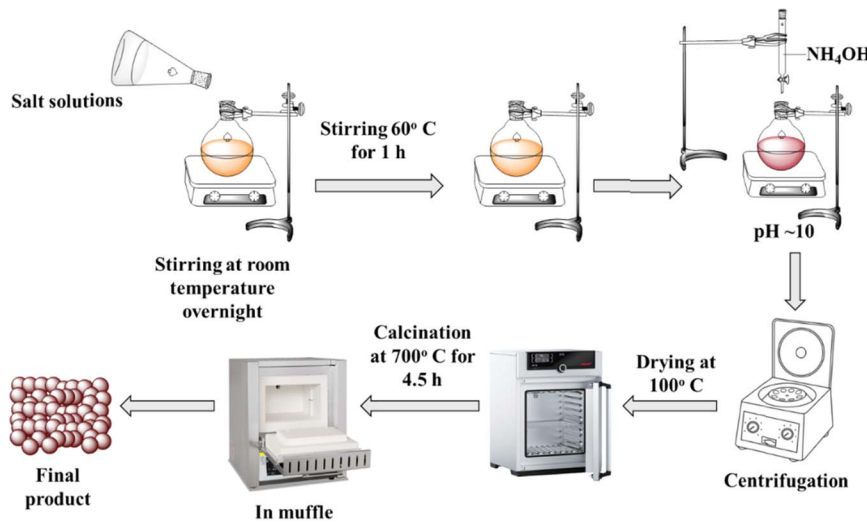


Fig. 1 Schematic representation for the synthesis of  $\text{Ni}_{0.6}\text{Cu}_{0.4}\text{Ce}_x\text{Fe}_{2-x}\text{O}_4$  ( $x = 0.0, 0.5, 1.0, 1.5$ ).

technique. The percent degradation of the CR dye by the catalyst was calculated using the formula below:<sup>27</sup>

$$\% \text{ Degradation} = \frac{C_0 - C_i}{C_0} \times 100 \quad (2)$$

where  $C_0$  is the initial concentration and  $C_i$  is the final concentration of dye solution at a given time interval.

The batch studies were carried out to optimize all degradation conditions, including the catalyst dose, CR solution concentration, pH, and light source variation. Catalyst dose variations of 30, 40, 50, 60, and 70 mg were tested in 50 mL of CR solution with concentration variations of 20, 30, 40, and 50 ppm at different pH values (4, 5, 6.5, 7, 8, and 9). The overall process is schematically represented in Fig. 2.

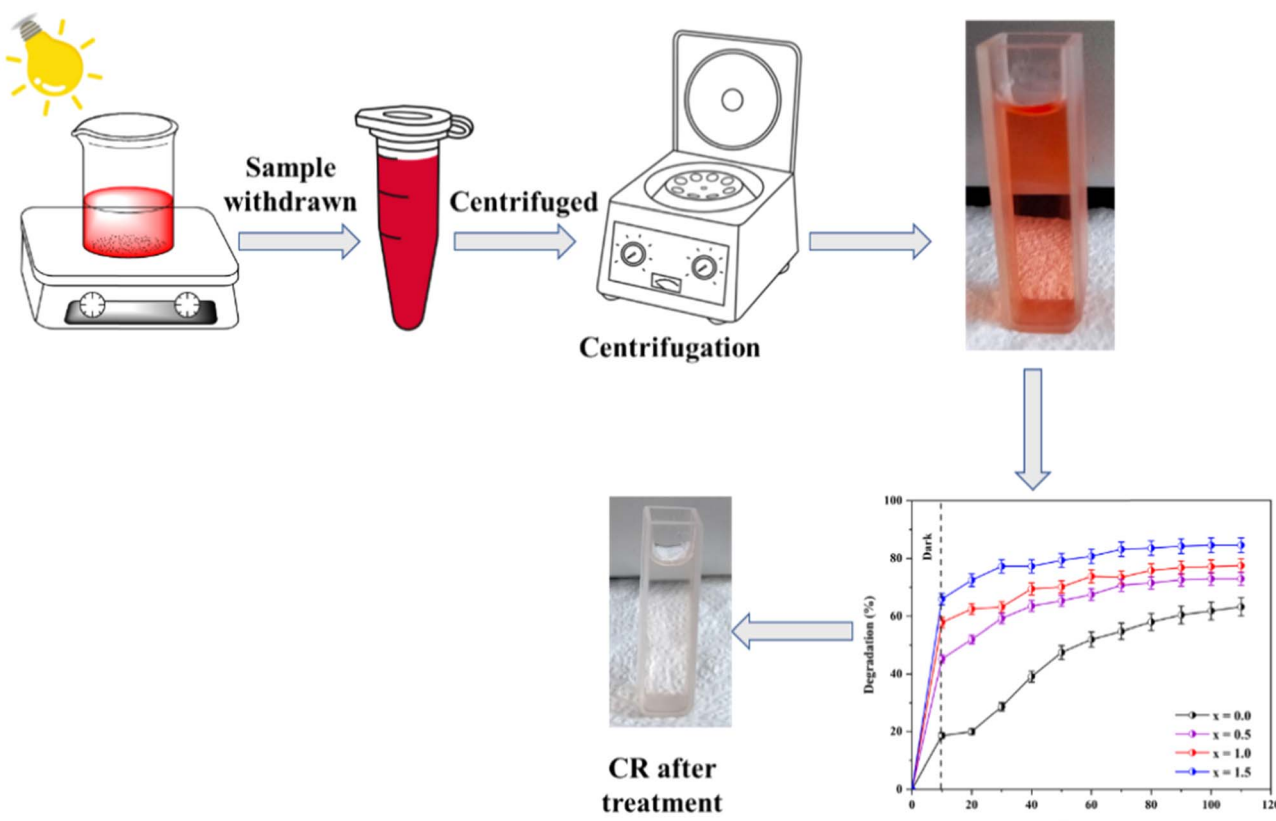


Fig. 2 Degradation procedure for CR dye using  $\text{Ni}_{0.6}\text{Cu}_{0.4}\text{Ce}_x\text{Fe}_{2-x}\text{O}_4$  ( $x = 0.0, 0.5, 1.0, 1.5$ ).

## 2.5. Analysis of scavenging effect on degradation

To investigate the photocatalytic activity mechanism of the photocatalyst, identifying the main reactive species is very crucial. The possible reactive species participating in the degradation could be  $h^+$ ,  $e^-$ ,  $HO^\cdot$ , or  $O_2^\cdot$ . Then, the radical scavenging test in the photodegradation was performed using 5 mM EDTA (for  $h^+$  scavenging),  $K_2Cr_2O_7$  (for  $e^-$  scavenging) and isopropyl alcohol (for  $HO^\cdot$  scavenging) individually. The degradation efficiency after 100 min was measured with 50 mL 40 ppm CR solution loaded with 60 mg of catalyst.<sup>28-31</sup>

## 3. Results and discussions

### 3.1. Fourier transform-infrared (FT-IR) spectroscopy

The FTIR spectrum (Fig. 3) exhibited two characteristic peaks at 552 and 357  $cm^{-1}$ , which are indicative of metal–oxygen bonds. Specifically, the vibration at 552  $cm^{-1}$  indicates the tetrahedral sites, while the signal at 357  $cm^{-1}$  represents the octahedral sites. These findings align with previous research identifying the signals as indicative of  $MFe_2O_4$  type spinel ferrite, suggesting the formation of a spinel ferrite composite without additional bonding.<sup>32</sup> It is worth noting that the intensity of the tetrahedral stretching vibration decreases with an increase in the  $Ce^{3+}$  ion concentration. Therefore, it can be predicted that with an increase of cerium content in the composition, the metal ions predominately orient into the octahedral voids of the crystal lattice. Consequently, this shift enhances the composite's catalytic properties, as the octahedral sites of the spinel ferrites are primarily responsible for their catalytic properties.<sup>33</sup> A characteristic peak near 2500  $cm^{-1}$  is obtained for  $CO_2$ . Similar spectral patterns for cerium-doped ferrites have been reported by Zakir *et al.* (2021).<sup>34</sup>

### 3.2. X-ray diffraction (XRD)

The XRD spectrum of  $Ni_{0.6}Cu_{0.4}Ce_xFe_{2-x}O_4$  ( $x = 0.0, 0.5, 1.0, 1.5$ ) shows well-defined and high intensity peaks (Fig. 4). In the

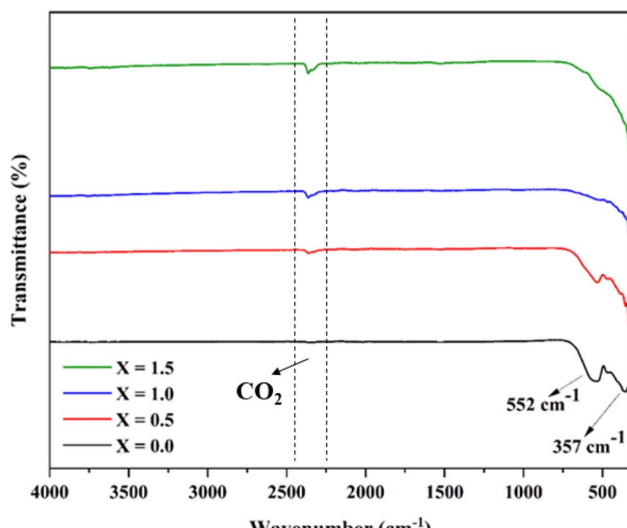


Fig. 3 FT-IR spectral pattern of  $Ni_{0.6}Cu_{0.4}Ce_xFe_{2-x}O_4$  ( $x = 0.0, 0.5, 1.0, 1.5$ ).

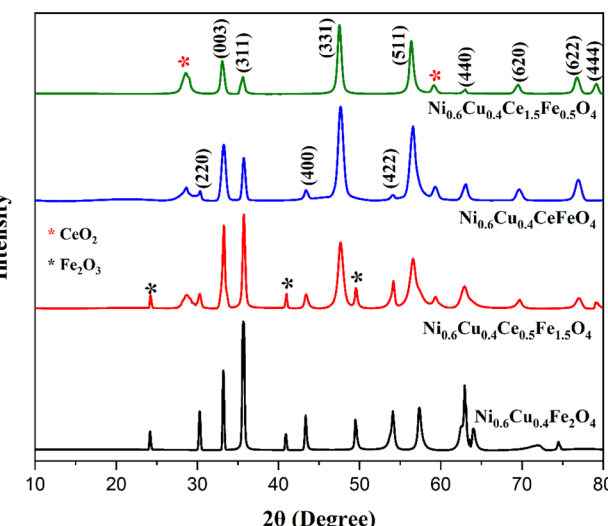


Fig. 4 XRD spectra for  $Ni_{0.6}Cu_{0.4}Ce_xFe_{2-x}O_4$  ( $x = 0.0, 0.5, 1.0, 1.5$ ).

figure, the sharp peaks correspond to the (220), (003), (311), (400), (331), (422), (511), (440), (533), (622), and (444) planes, in accordance with JCPDS cards (011-6755) and (22-1086), confirming the successful formation of spinel ferrite.<sup>35,36</sup> Additionally, there are peaks at  $2\theta = 24.1^\circ, 40.85^\circ$ , and  $49.46^\circ$ , corresponding to the  $\alpha$ - $Fe_2O_3$  phase. An additional peak appears at  $56.29^\circ$  that corresponds to  $CeO_2$ , which is possibly due to insufficient reaction. A similar XRD pattern was also reported.<sup>35</sup>

The crystallite size was calculated by the Scherrer formula using the full width at half maxima (FWHM) values of each corresponding peaks.

$$D = \frac{k\lambda}{\beta \cos \theta} \quad (3)$$

where  $k$  is the Scherrer constant (0.89 for polycrystalline material),  $\lambda$  is the wavelength of the X-ray (0.1542 nm),  $\beta$  is the FWHM of the corresponding peaks (in radians),  $\theta$  is the Bragg's diffraction angle, and  $D$  is the average crystallite size.<sup>37</sup>

The lattice parameter, which is the edge length of the unit cell in three different axes, was calculated using the formula for a cubic spinel where the lengths of the three edges are equal:

$$a = d_{hkl} \times \sqrt{h^2 + k^2 + l^2} \quad (4)$$

The  $d$ -spacing ( $d_{hkl}$ ) is calculated from Bragg's law.

$$2d_{hkl} \sin \theta = \lambda$$

Table 1 Data for XRD analysis of  $Ni_{0.6}Cu_{0.4}Ce_xFe_{2-x}O_4$

Cerium content ( $X$ )	Average crystallite size, $D$ (nm)	Average lattice parameter, $a$ ( $\text{\AA}$ )	X-ray density, $p$ ( $\text{g cm}^{-3}$ )
$X = 0.0$	38.19	8.310	5.47
$X = 0.5$	19.48	8.308	6.45
$X = 1.0$	16.15	8.302	7.44
$X = 1.5$	18.83	8.158	8.87



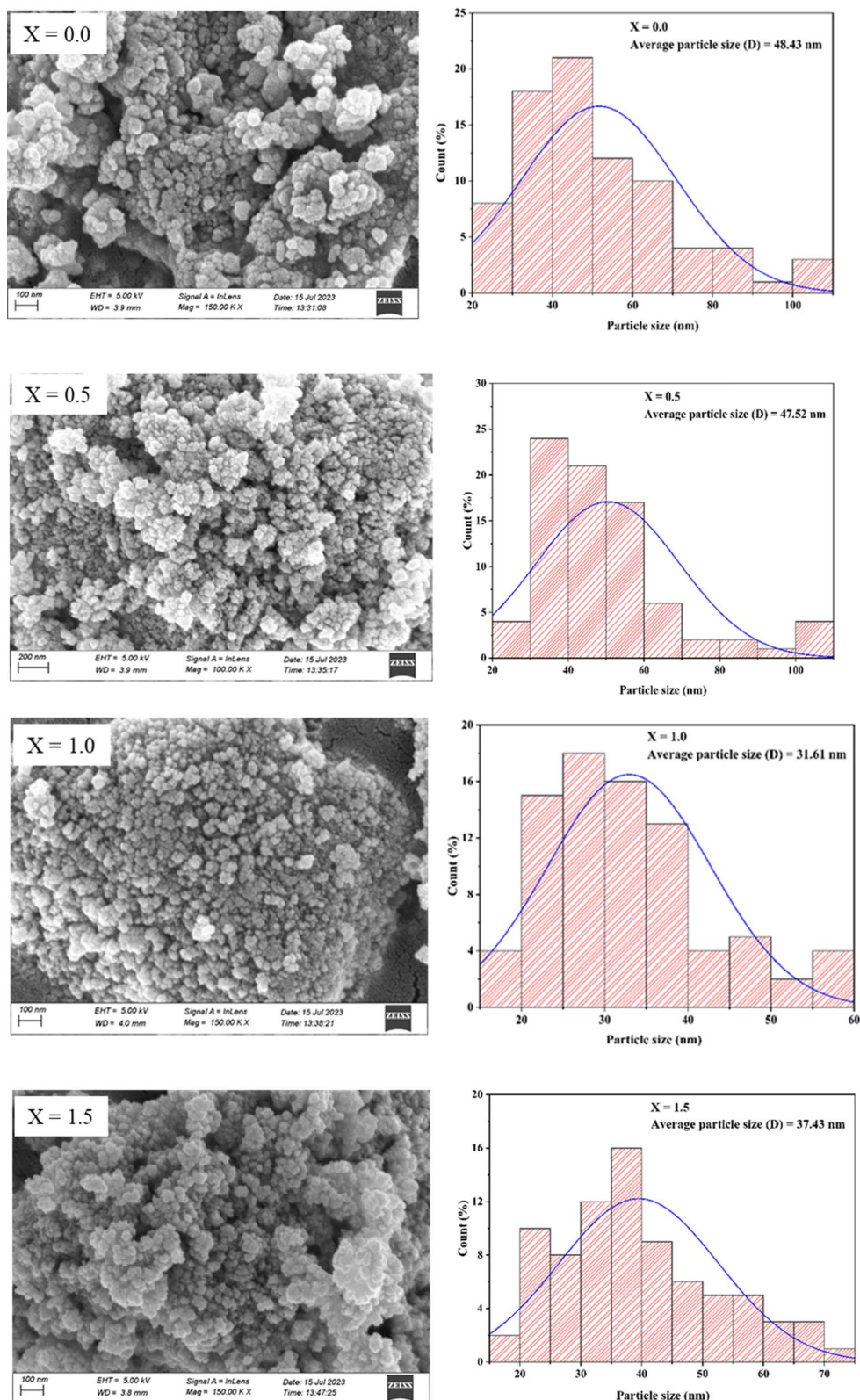


Fig. 5 SEM images with histogram for  $\text{Ni}_{0.6}\text{Cu}_{0.4}\text{Ce}_x\text{Fe}_{2-x}\text{O}_4$  ( $x = 0.0, 0.5, 1.0, 1.5$ ).

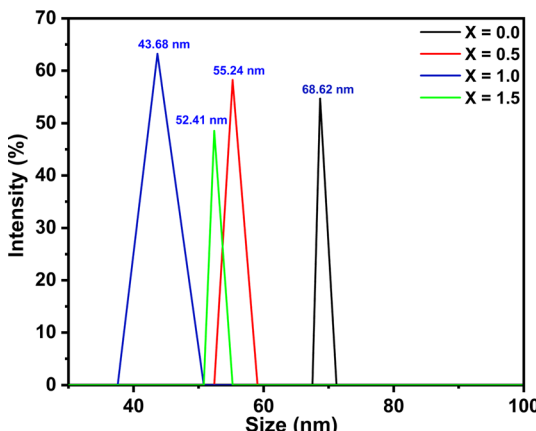


Fig. 6 DLS measurement for  $\text{Ni}_{0.6}\text{Cu}_{0.4}\text{Ce}_x\text{Fe}_{2-x}\text{O}_4$  ( $x = 0.0, 0.5, 1.0, 1.5$ )

$$d_{hkl} = \frac{\lambda}{2 \sin \theta} \quad (5)$$

The values of the lattice parameter closely match those reported in the literature.<sup>35,38</sup>

The X-ray density ( $\rho_x$ ) was calculated using the formula:

$$\rho_x = \frac{ZM}{Na^3} \quad (6)$$

where  $Z$  is the number of atoms per unit cell (8 for spinel ferrite),  $M$  is the molecular weight of the composite,  $N$  is Avogadro's number, and  $a$  is the lattice parameter of the composite in cm.

Since  $\text{Ce}^{3+}$  has larger ionic radii compared to  $\text{Fe}^{3+}$ , it may expect to increase the crystallite size of the ferrite with gradual insertion of cerium (Table 1). Nevertheless, from  $x = 0.0$  to  $x = 1.0$ , the crystallite size was decreased as the  $\text{Ce}^{3+}$  concentration increased because the crystallite size of the ferrite was influenced mostly by the cationic distribution rather than the ionic radii. Certainly, this larger ionic size imparted a positive effect on the crystallite size by hindering the crystal growth of the ferrite.<sup>15</sup> However, at  $x = 1.5$ , the crystallite size slightly increased. This can be attributed to the different concentrations. At lower concentrations, crystal growth is controlled and hindered. Conversely, at higher  $\text{Ce}^{3+}$  concentration, it favors crystal formation near the nucleation center, resulting in increased crystallite size.<sup>39</sup> The X-ray density also increased with the increase in  $\text{Ce}^{3+}$  content. This is because the molecular weight and density of the  $\text{Ce}^{3+}$  ion are higher than those of the  $\text{Fe}^{3+}$  ion.

### 3.3. Surface morphology and elemental analysis

Surface morphology analysis of the synthesized materials was performed using field-emission scanning electron microscopy (FE-SEM), where the well-distributed particles were observed. The analysis was performed using ImageJ to determine the average particle size by the distribution histogram to the log-normal distribution function, as reported (Fig. 5).<sup>40</sup>

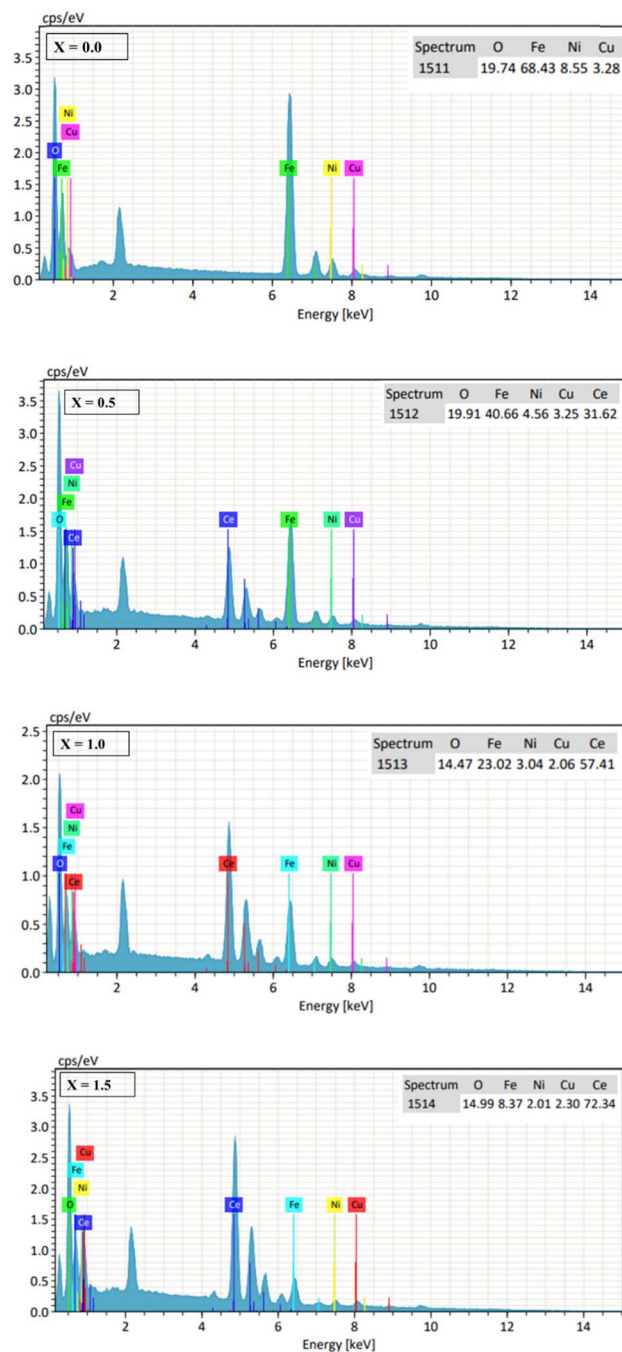


Fig. 7 EDX spectra for  $\text{Ni}_{0.6}\text{Cu}_{0.4}\text{Ce}_x\text{Fe}_{2-x}\text{O}_4$  ( $x = 0.0, 0.5, 1.0, 1.5$ ).

$$f(D) = \left( \frac{1}{\sqrt{2\pi} \cdot \sigma_D} \right) \exp \left[ \frac{\ln^2 \left( \frac{D}{D_0} \right)}{2\sigma^2} \right] \quad (7)$$

where  $f(D)$  is the size distribution function,  $\sigma_D$  is the standard deviation,  $D_0$  is the mean of logarithmic values,  $\sigma$  is the variance and  $D$  is the average particle size, which was found to be 48.43, 47.52, 31.61, and 37.43 nm, respectively, from the histogram for the particle distribution of  $\text{Ni}_{0.6}\text{Cu}_{0.4}\text{Ce}_x\text{Fe}_{2-x}\text{O}_4$  ( $x = 0.0, 0.5, 1.0$ , and  $1.5$ ). The result indicates that the particle size decreases

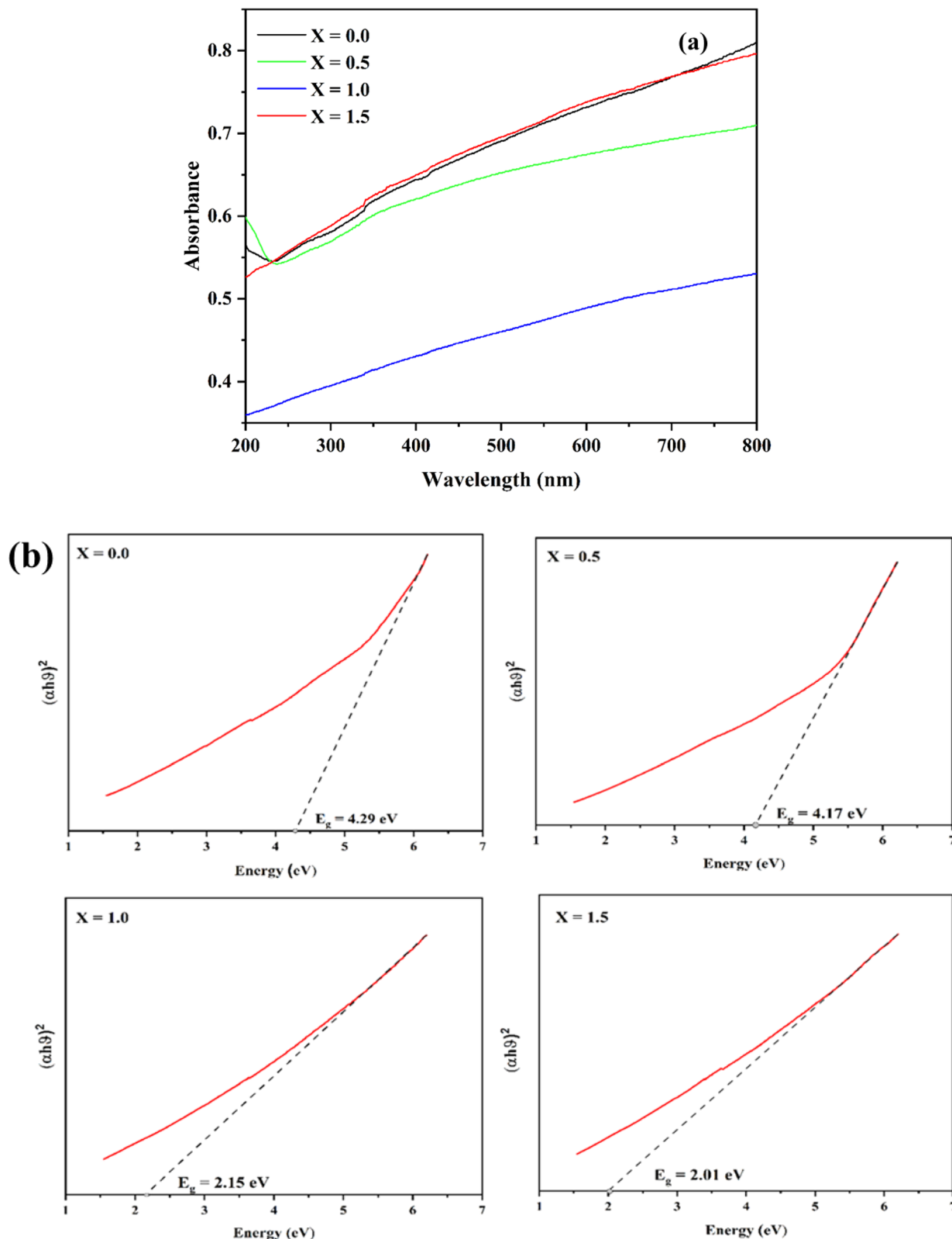


Fig. 8 (a) UV-visible spectra and (b) Tauc plot for band gap analysis of  $\text{Ni}_{0.6}\text{Cu}_{0.4}\text{Ce}_x\text{Fe}_{2-x}\text{O}_4$  ( $x = 0.0, 0.5, 1.0, 1.5$ ).

with the insertion of cerium ion, while it was observed that the particles have formed agglomeration. The particle size results from the SEM analysis correlate with the crystallite size values

obtained from XRD analysis. To support the data, dynamic light scattering (DLS) was also analyzed using Malvern ZS Xplorer, which suggested that the size ranges from 68.62 to 43.68 nm

(Fig. 6). The elemental composition of  $\text{Ni}_{0.6}\text{Cu}_{0.4}\text{Ce}_x\text{Fe}_{2-x}\text{O}_4$  ( $x = 0.0, 0.5, 1.0, 1.5$ ) was investigated by EDX spectra (Fig. 7), where the spectra demonstrate the presence of all elements in ferrite. One additional peak in all four spectra at near 2 keV is due to the gold coating during the sample preparation of FE-SEM, as gold shows the characteristic peak at this region in the EDX spectrometric analysis.<sup>39,41</sup>

### 3.4. Band gap

The band gap energy of ferrites plays a crucial role in their photocatalytic performance. Materials with a higher band gap value have limited photocatalytic performance due to their ability to exploit lesser amount of photon energy for their electronic excitation and transition.<sup>42</sup> Lowering the band gap indicates that the electronic transition from the valence band (VB) to the conduction band (CB) requires less energy, thus promoting the formation of an electron-hole pair ( $e^-/h^+$ ) and consequently enhancing the photocatalytic performance of the catalyst (Fig. 8a). The band gap values of the catalysts were calculated using the Tauc equation:

$$(\alpha h\nu)^n = \beta(h\nu - E_g) \quad (8)$$

Here,  $n$  is 1/2 or 2 for an indirect or direct band gap value, respectively.<sup>43</sup> The band gap obtained from the plot of  $(\alpha h\nu)^2$  versus photon energy ( $h\nu$ ) indicates the decrease in direct band gap from 4.29 eV for the undoped sample to 2.01 eV for the highest cerium doping (Fig. 8b).

### 3.5. Vibrating sample magnetometer (VSM) analysis

The VSM data were used to analyze the magnetic hysteresis loop. The loop was plotted with the magnetic moment ( $\text{emu g}^{-1}$ ) versus the applied magnetic field,  $H$  (Oe) data obtained at 300 K (Fig. 9). The hysteresis curve shows a slightly narrower

Table 2 Data for VSM analysis of  $\text{Ni}_{0.6}\text{Cu}_{0.4}\text{Ce}_x\text{Fe}_{2-x}\text{O}_4$

Content	$M_S$ (emu g <sup>-1</sup> )	$M_R$ (emu g <sup>-1</sup> )	$H_C$ (Oe)
$X = 0.0$	22.61	0.63	29.02
$X = 0.5$	12.94	8.99	594.93
$X = 1.0$	11.64	9.22	1094.39
$X = 1.5$	4.57	2.67	428.01

loop with moderately smaller values of saturation magnetization ( $M_S$ ) and magnetic remanence ( $M_R$ ), which indicates the material as a soft magnetic ferrite.<sup>44,45</sup>

The values of the magnetic remanence ( $M_R$ ) and coercivity ( $H_C$ ) increased with the increase of  $\text{Ce}^{3+}$  up to  $x = 1.0$ , while the values then decreased for  $x = 1.5$  (Table 2). The highest coercivity has been observed for  $\text{Ni}_{0.6}\text{Cu}_{0.4}\text{CeFeO}_4$ , with a comparatively wider hysteresis loop. This reveals that it is the harder magnet with a greater value of cerium-doped spinel ferrites obtained by the coprecipitation method reported earlier.<sup>38</sup>

### 3.6. Photocatalytic degradability

**3.6.1. Efficiency of catalyst.** The catalytic performance of the synthesized  $\text{Ni}_{0.6}\text{Cu}_{0.4}\text{Ce}_x\text{Fe}_{2-x}\text{O}_4$  ( $x = 0.0, 0.5, 1.0, 1.5$ ) nanocomposites has been studied using 50 mg of the catalyst for 50 mL of 20 ppm solution of CR dye (Fig. 10a).

The photocatalytic activity of undoped  $\text{Ni}_{0.6}\text{Cu}_{0.4}\text{FeO}_4$  ( $x = 0.0$ ) was only 63.18% with the above-applied condition, which has gradually increased with the increase in the amount of  $\text{Ce}^{3+}$  in the catalyst. The activity has increased to 72.88% with the increase of  $\text{Ce}^{3+}$  ( $x = 0.5$ ). The further increase of  $\text{Ce}^{3+}$  ( $x = 1.0$ ) has shown 77.45% of degradation, while the highest activity (84.51%) has been observed with the maximum  $\text{Ce}^{3+}$  concentration ( $x = 1.5$ ). The activity series of the catalyst can be written as  $\text{Ni}_{0.6}\text{Cu}_{0.4}\text{FeO}_4 < \text{Ni}_{0.6}\text{Cu}_{0.4}\text{Ce}_{0.5}\text{Fe}_{1.5}\text{O}_4 < \text{Ni}_{0.6}\text{Cu}_{0.4}\text{CeFeO}_4 < \text{Ni}_{0.6}\text{Cu}_{0.4}\text{Ce}_{1.5}\text{Fe}_{0.5}\text{O}_4$ . The obtained result can be explained based on XRD, SEM, band gap and FTIR analysis. In the XRD and SEM analysis,  $\text{Ni}_{0.6}\text{Cu}_{0.4}\text{Ce}_{1.5}\text{Fe}_{0.5}\text{O}_4$  ( $X = 1.5$ ) has a larger particle size than  $\text{Ni}_{0.6}\text{Cu}_{0.4}\text{CeFeO}_4$  ( $X = 1.0$ ), with a reduced band gap value, as shown from the FTIR analysis of the catalyst.  $X = 1.5$  exhibits enhanced cationic occupation in the octahedral void of the crystal structure, which contributed to the improved catalytic performance.

Therefore, it can be concluded that the doping of  $\text{Ce}^{3+}$  into the  $\text{Ni}_{0.6}\text{Cu}_{0.4}\text{FeO}_4$  spinel ferrite has a positive influence on the photocatalytic degradation of CR.

**3.6.2. Effect of the dose and concentration.** The optimum dose for the best-suited catalyst has been studied by performing the same experiment with different doses of  $\text{Ni}_{0.6}\text{Cu}_{0.4}\text{Ce}_{1.5}\text{Fe}_{0.5}\text{O}_4$  (40, 50, 60, and 70 mg), for 50 mL of 20 ppm CR solution (Fig. 10b). It was found that the catalytic activity has been increased with the increase of the dose from 40 mg (72.75%) to 50 mg (84.51%). The highest activity was observed with a 60 mg dose of the catalyst (86.80%), but a further increase in dose to 70 mg resulted in a decrease in the activity to 80.19%. Catalytic doses higher than 60 mg present in the definite volume of dye solution gradually increased the agglomeration rate of the catalyst, which reduced the available surface area of the catalyst to adsorb the dye

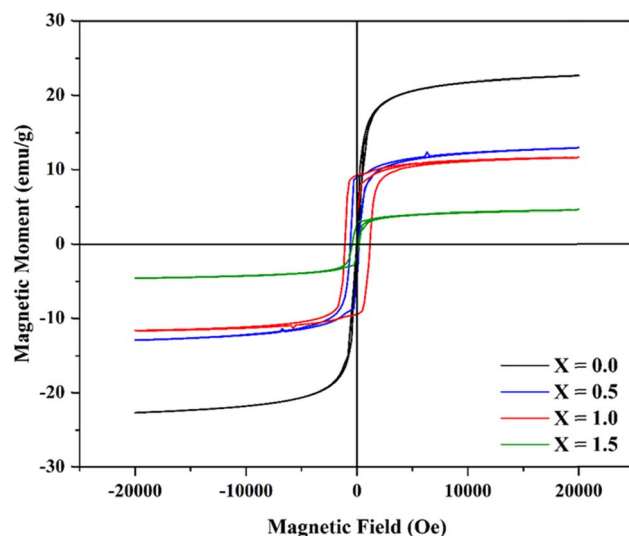


Fig. 9 Hysteresis loop obtained at 300 K for  $\text{Ni}_{0.6}\text{Cu}_{0.4}\text{Ce}_x\text{Fe}_{2-x}\text{O}_4$  ( $x = 0.0, 0.5, 1.0, 1.5$ ).



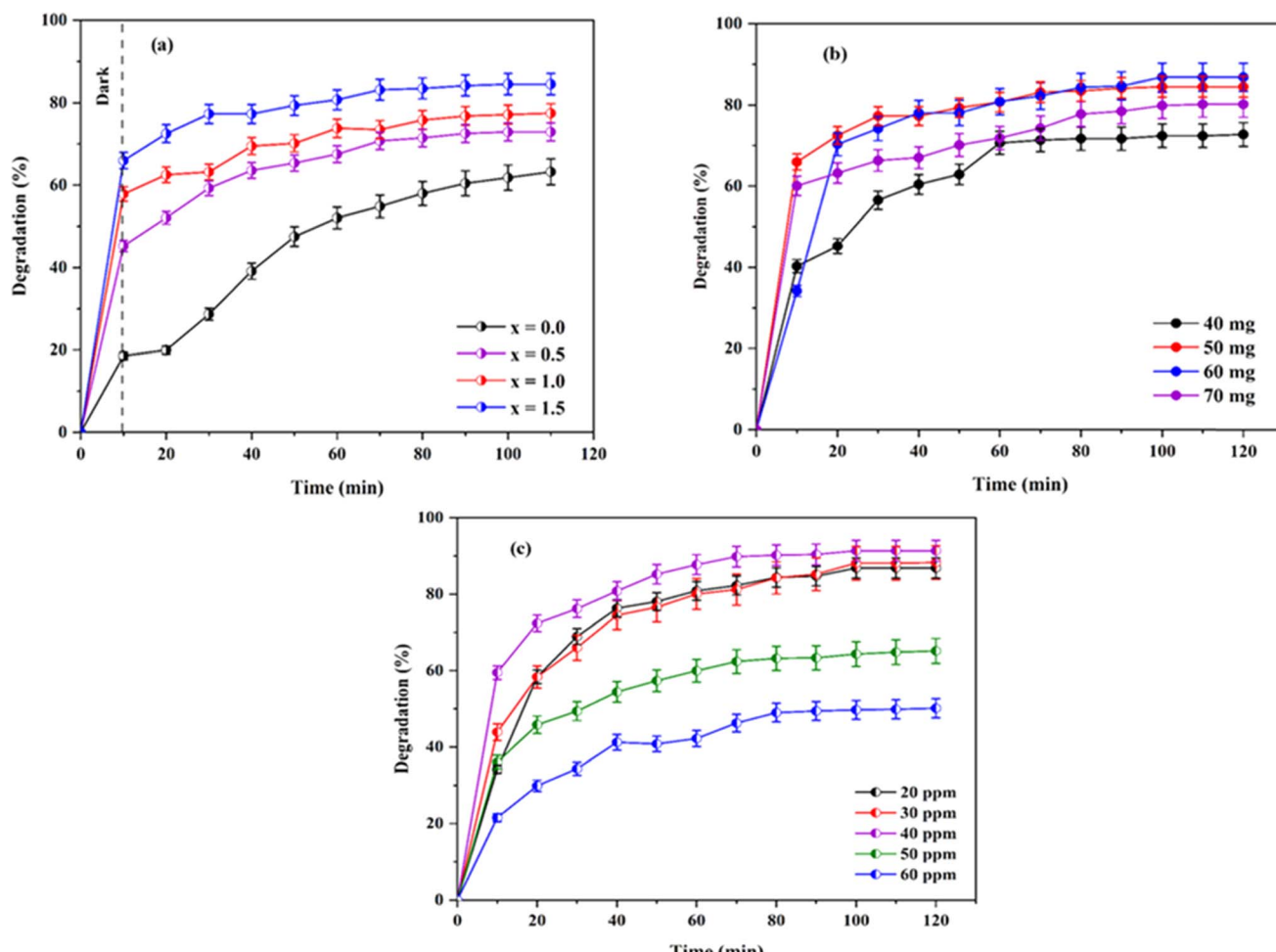


Fig. 10 (a) Efficiency of the catalyst, (b) effect of the dosage, and (c) effect of the concentration on the degradation.

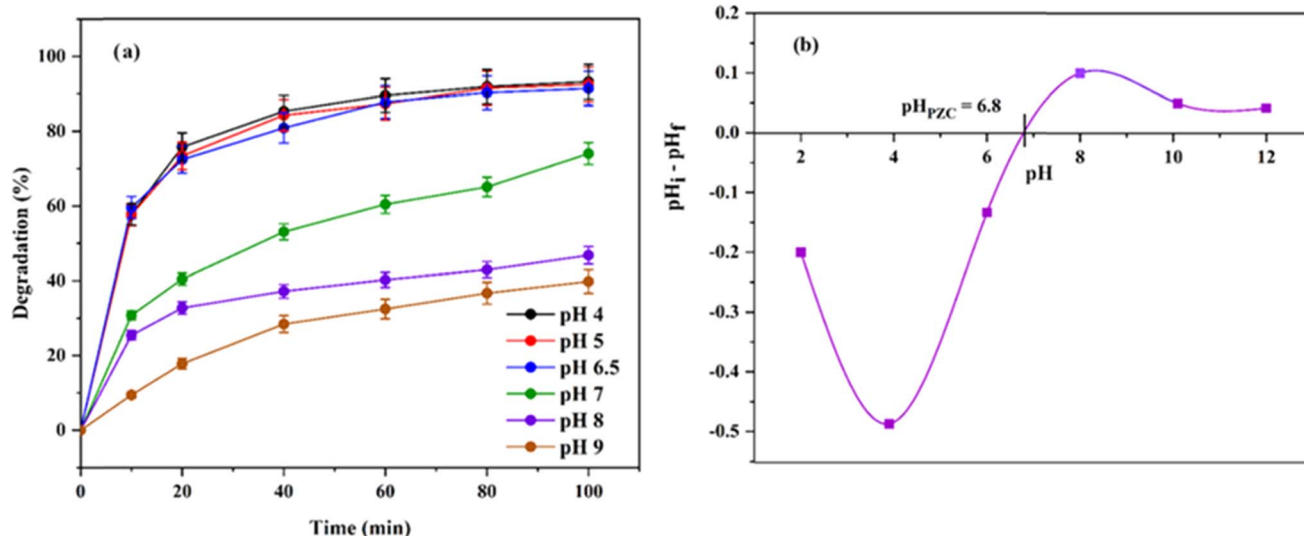


Fig. 11 (a) Effect of pH on the degradation efficiency. (b) Point of zero charge for  $\text{Ni}_{0.6}\text{Cu}_{0.4}\text{Ce}_{1.5}\text{Fe}_{0.5}\text{O}_4$ .

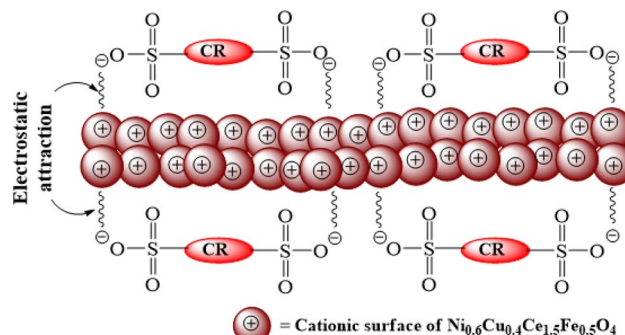


Fig. 12 Schematic representation of the electrostatic attraction between the cationic surface of the catalyst with the anionic CR.

molecule. Along with this, the turbidity of the solution increased due to the higher catalyst dose reducing the penetration of light through the solution to the surface of the catalyst. As a result, the amount of reactive species formation decreased.<sup>46</sup>

Following that, an experiment was carried out to optimize the concentration of CR to get the best catalyst performance using 60 mg of  $\text{Ni}_{0.6}\text{Cu}_{0.4}\text{Ce}_{1.5}\text{Fe}_{0.5}\text{O}_4$  per 50 mL CR solutions (Fig. 10c). Here, the degradation efficiency has increased with the increase of concentration of CR solution from 20 ppm (86.80%) to 30 ppm (88.08%). Moreover, the highest activity was observed with 40 ppm (91.34%) of CR solution, but the degradation efficiency decreased with a further increase of concentration to 50 ppm (65.15%) and 60 ppm (50.13%). With the higher dye concentration above 40 ppm, the formation of the reactive species from the catalyst surface is also reduced due to increased interaction between the dye molecules with light at higher dye concentration.<sup>46,47</sup> Therefore, the results obtained from the study of the dose and concentration are correlated. There must be a suitable catalyst dose-to-concentration ratio that is required to observe the maximum degradation rate by the photocatalyst.

In this study, the optimized dose and concentration were observed to be 60 mg of 40 ppm CR in 50 mL solution.

**3.6.3. Effect of pH.** At the catalyst dose of 60 mg and CR concentration of 40 ppm, the impact of the initial solution pH on the CR degradation was also studied. The natural pH of the CR solution was found to be 6.5, which was the pH value at which the abovementioned studies were carried out. Moreover, the pH ranges of 4.0, 5.0, 7.0, 8.0, and 9.0 were used for various investigations. The degradation ratio of CR is shown to sparingly vary. It maintains a high level below pH 7.0, and then gradually falls from pH 7.0 to higher (Fig. 11a). Thus, working at a natural pH of 40 ppm CR solution for their photocatalytic degradation can easily be adopted.

The variation in the degradability is due to the change in adsorption behavior of the catalyst at different pH values. The adsorption-desorption processes are influenced by the alteration of the nature of the electrical double layer of the particle interface.<sup>48</sup> The obtained result can be explained as follows. At low pH, the positive surface of the catalyst facilitates the degradation efficiency due to the electrostatic affinity of the catalyst towards anionic CR dye. Furthermore, at a high pH value, the surface gets a charge similar to the anionic CR, which repels the dye molecules from the vicinity of the catalyst surface. Thus, the adsorption of dye molecules is reduced, consequently decreasing the degradation percentage. The process is depicted schematically in Fig. 12.

The result can be evident from the point of zero charge (PZC) study of  $\text{Ni}_{0.6}\text{Cu}_{0.4}\text{Ce}_{1.5}\text{Fe}_{0.5}\text{O}_4$ , which is  $\text{pH}_{\text{PZC}} = 6.8$ , and supports the outcome mentioned above in this section (Fig. 11b). PZC commonly states that at  $\text{pH} < \text{pH}_{\text{PZC}}$ , the surface of the solid material is positively charged, and *vice versa*. Thus, CR is an anionic dye that can be adsorbed best to a surface having an opposite charge. Hence, in this study, the catalytic activity was highly maintained below pH 7.0. The CR anions were, however, typically excluded away from the similarly charged catalyst surface at higher pH levels. Consequently, the degradation ratio then started to decrease. Similar results have

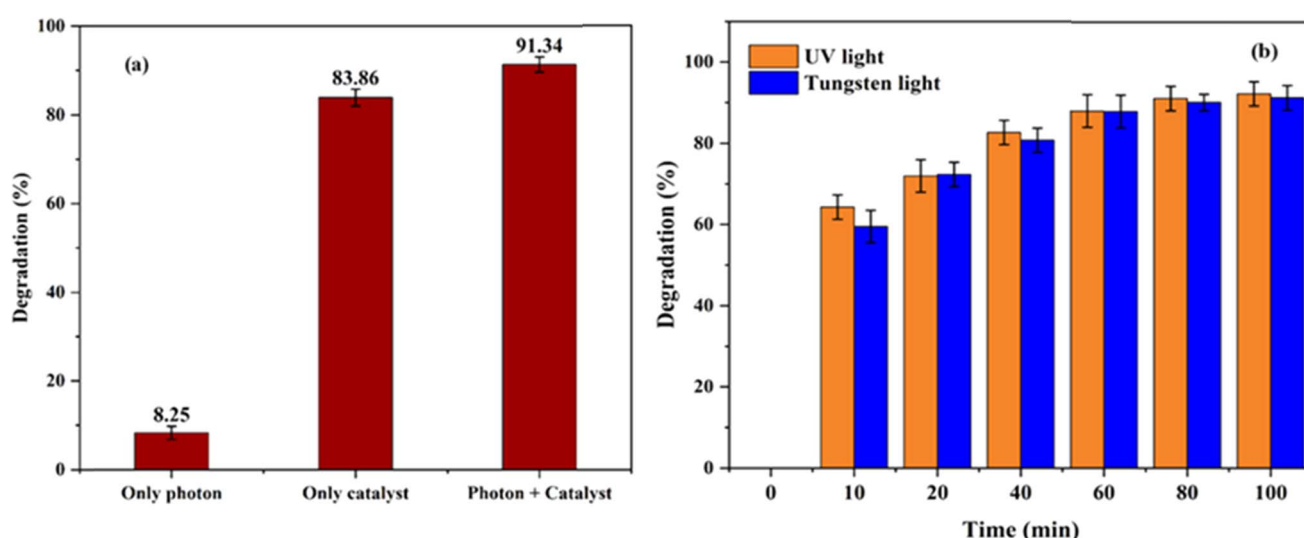


Fig. 13 (a) Effect of light and catalyst, and (b) effect of various light sources on degradation.

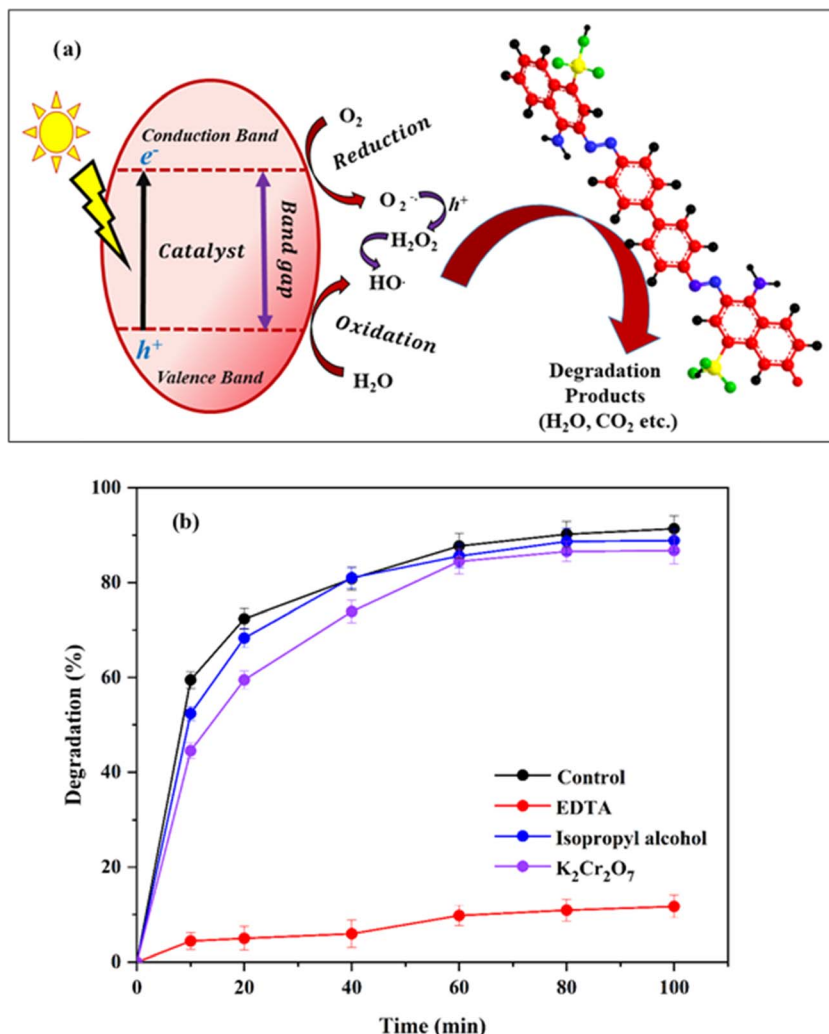


Fig. 14 (a) Schematic representation of the degradation mechanism of CR by  $\text{Ni}_{0.6}\text{Cu}_{0.4}\text{Ce}_x\text{Fe}_{2-x}\text{O}_4$  under light energy. (b) Role of different scavengers on quenching the degradation percentage.

been reported describing the effect of the initial solution pH on the degradation of CR.<sup>49,50</sup>

**3.6.4. Effect of light and catalyst on degradation.** To carry out the photodegradation process for CR, understanding the influence of light and catalyst on the degradation system is very important.

The experiment carried out using 60 mg of  $\text{Ni}_{0.6}\text{Cu}_{0.4}\text{Ce}_{1.5}\text{Fe}_{0.5}\text{O}_4$  catalyst for 50 mL of 40 ppm dye with CR under visible light radiation with no catalyst showed only 8.25% degradation, while the catalyst alone with no light showed 83.86% removal (Fig. 13a). Hence, it can be concluded that the synergistic effect of light with the catalyst yields an excellent

Table 3 Comparison table for the degradation efficiency of the as-synthesized nanocatalyst

Catalyst	Synthesis method	Crystallite size	Treated dye	Optimum dose	Optimum concentration	Optimum pH	Efficiency	Ref.
NiO	Coprecipitation	41 nm	Congo red	20 mg	10 ppm	4	72%	51
Ag-CdS@Pr-TiO <sub>2</sub>	Sol-gel	28.32 nm	Methyl orange	2 $\mu\text{g}$	32 $\text{mg L}^{-1}$	—	98%	52
CoFe <sub>2</sub> O <sub>4</sub>	Coprecipitation	44.26 nm	Methylene blue	—	—	—	74%	53
GO/CuFe <sub>2</sub> O <sub>4</sub>	Precipitation	2.221 Å	Malachite green	—	—	—	62%	54
fs-CoFe <sub>2</sub> O <sub>4</sub>	Coprecipitation	5.26 nm	Congo red	35 mg	5 ppm	9	91%	46
Co <sub>0.6</sub> Zn <sub>0.1</sub> Ni <sub>0.3</sub> Ce <sub>0.15</sub> Fe <sub>1.85</sub> O <sub>4</sub>	Sol-gel auto combustion	38 nm	Congo red	—	—	Up to 7	94.50%	55
Ni <sub>0.6</sub> Cu <sub>0.4</sub> Ce <sub>1.5</sub> Fe <sub>0.5</sub> O <sub>4</sub>	Coprecipitation	18.83 nm	Congo red	60 mg	40 ppm	Up to 6.5	91%	Present work

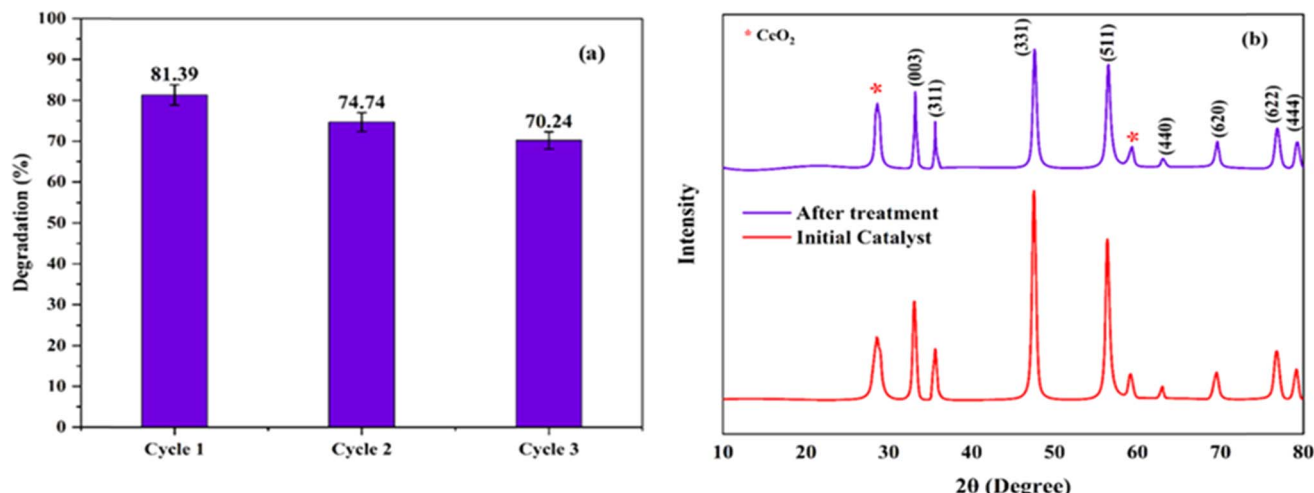


Fig. 15 (a) Recyclability of  $\text{Ni}_{0.6}\text{Cu}_{0.4}\text{Ce}_{0.4}\text{Fe}_{2-x}\text{O}_4$ , and (b) XRD spectra of  $\text{Ni}_{0.6}\text{Cu}_{0.4}\text{Ce}_{0.4}\text{Fe}_{2-x}\text{O}_4$  before and after treatment.

result of 91.34% degradation of the toxic CR dye in aqueous solution.

**3.6.5. Variation of light source.** The light source has an influence on the efficiency of catalytic degradation of CR dye. Therefore, the obtained experimental result of 60 mg catalyst in 40 ppm CR solution in tungsten light was compared with a UV light source (Fig. 13b). The study with UV radiation showed a slight increase in the activity of the catalyst (92.30%) compared to the tungsten light source (91.34%).

This may be attributed to the higher energy of the radiation in UV light compared to other lights, leading to higher degradation efficiency.

**3.6.6. Scavenging effect on active species.** The scavenging test was performed using 5 mM solution of EDTA ( $\text{h}^+$  scavenger),  $\text{K}_2\text{Cr}_2\text{O}_7$  ( $\text{e}^-$  scavenger), and isopropyl alcohol ( $\text{HO}^\cdot$  scavenger)<sup>30</sup> under the optimum conditions established of 50 mL solution of CR loaded with 60 mg of catalyst (Fig. 14b). It has been observed that the degradation efficiency has been significantly quenched

by EDTA (11.70%), revealing the hole ( $\text{h}^+$ ) as the primary active species performing the degradation of CR. Furthermore,  $\text{K}_2\text{Cr}_2\text{O}_7$  and isopropyl alcohol minimize the degradation at a lower scale of 86.73% and 88.84%, indicating that  $\text{e}^-$  and  $\text{HO}^\cdot$  also have some function as the active species in the degradation process, respectively. Thus, the overall process can be represented schematically as follows (Fig. 14a). Table 3 illustrates a comparison table for the degraded efficiency of the produced nanocatalyst.

**3.6.7. Recyclability and stability of  $\text{Ni}_{0.6}\text{Cu}_{0.4}\text{Ce}_{1.5}\text{Fe}_{0.5}\text{O}_4$ .** The recyclability of  $\text{Ni}_{0.6}\text{Cu}_{0.4}\text{Ce}_{1.5}\text{Fe}_{0.5}\text{O}_4$  was evaluated for three cycles (Fig. 15a). The particles were collected, washed with water and ethanol, and then dried in an oven at 100 °C for the successive test of recyclability of  $\text{Ni}_{0.6}\text{Cu}_{0.4}\text{Ce}_{1.5}\text{Fe}_{0.5}\text{O}_4$ . The catalyst showed a degradation percentage of 81.39%, 74.74%, and 70.24% after the first, second, and third cycles, respectively, indicating the catalyst as a good candidate for recycling. XRD measurements were performed on the catalyst after three cycles of recycling to determine if there was any structural change after

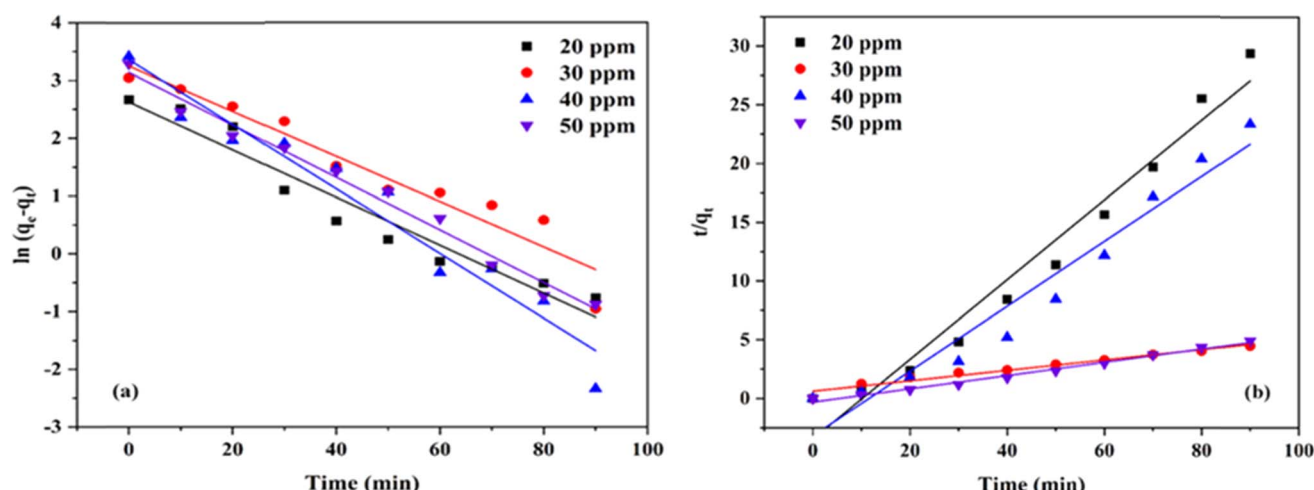


Fig. 16 Plots for the (a) pseudo-first-order and (b) pseudo-second-order kinetic models.



Table 4 Data for the pseudo-first-order and pseudo-second-order kinetic studies

Concentration (ppm)	Pseudo-first-order			Pseudo-second-order		
	$q_e$ (mg g <sup>-1</sup> )	$k_1$ (min <sup>-1</sup> )	$R^2$	$q_e$ (mg g <sup>-1</sup> )	$k_2$ (g mg <sup>-1</sup> min <sup>-1</sup> )	$R^2$
20	13.86	0.00046	0.9445	15.50	0.00416	0.9811
30	25.81	0.00044	0.9288	22.47	0.00198	0.9644
40	28.82	0.00062	0.9485	31.45	0.00101	0.9953
50	23.14	0.00051	0.9839	28.09	0.00127	0.9893

recovery. The result (Fig. 15b) demonstrates that the catalyst is highly stable and suitable for recycling.

### 3.7. Kinetic model

The study of adsorption kinetics gives critical information regarding the degradation mechanism. In this study, pseudo-first-order and pseudo-second-order models were used to assess the adsorption kinetics. Lagergren's pseudo-first-order kinetic model, which describes the physisorption between the adsorbent and adsorbate, can be represented in the linear form as follows:<sup>56</sup>

$$\ln(q_e - q_t) = \ln(q_e) - \frac{k_1}{2.303} t \quad (9)$$

Moreover, the linear form of the rate equation for the pseudo-second-order kinetic model can be written as follows:

$$\frac{t}{q_t} = \frac{1}{k_2 q_e^2} + \frac{t}{q_e} \quad (10)$$

where  $q_e$  and  $q_t$  (mg g<sup>-1</sup>) are the adsorption capacities at equilibrium and time  $t$  (sec), respectively. Moreover,  $k_1$  (min<sup>-1</sup>) and  $k_2$  (g mg<sup>-1</sup> min<sup>-1</sup>) are the pseudo-first-order and pseudo-second-order rate constants, respectively.

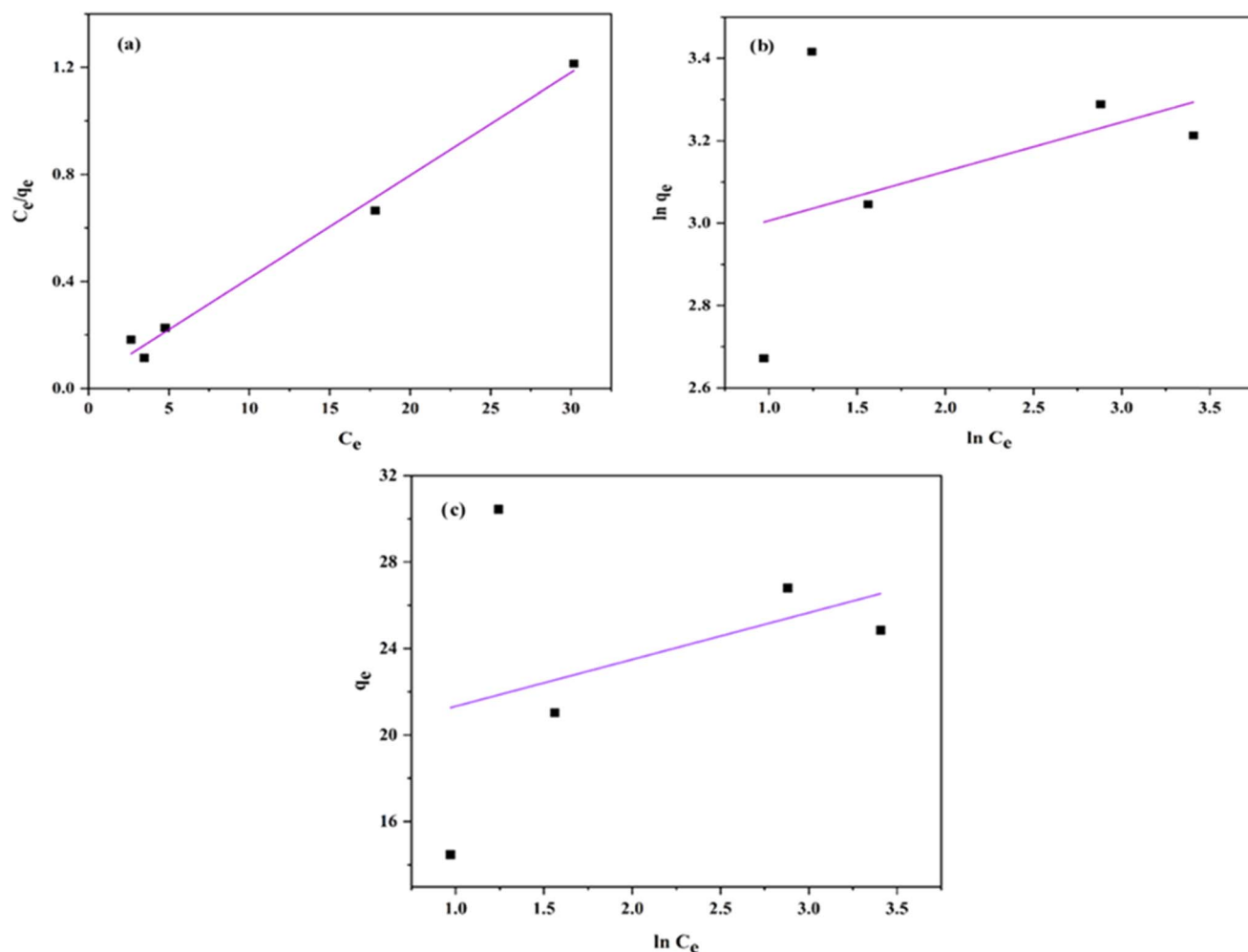


Fig. 17 Plots for the (a) Langmuir, (b) Freundlich, and (c) Temkin isotherm models.

Table 5 Data for the analysis of different isotherm models

Langmuir			Freundlich			Temkin		
$q_m$ (mg g <sup>-1</sup> )	$K_L$ (L mg <sup>-1</sup> )	$R^2$	$n$	$K_F$	$R^2$	$B$ (J mol <sup>-1</sup> )	$K_T$ (L g <sup>-1</sup> )	$R^2$
26.04	1.37	0.9903	8.35	17.9215	0.1986	2.169	6.84	0.1448

The plot of the kinetic model for CR on  $\text{Ni}_{0.6}\text{Cu}_{0.4}\text{Ce}_{1.5}\text{Fe}_{0.5}\text{O}_4$  is represented in Fig. 16a and b, and the values are tabulated in Table 4. Considering the correlation coefficient ( $R^2$ ) values for both models, it can be said that the process follows pseudo-second-order kinetics rather than the pseudo-first-order kinetics. As a result, the rate-determining step followed the chemisorption process.

### 3.8. Isotherm analysis

The adsorption isotherm was also evaluated to understand the degradation behavior of CR with the synthesized catalyst using the Langmuir, Freundlich, and Temkin models. Those can be expressed in the linear form as follows:<sup>56,57</sup>

$$\frac{C_e}{q_e} = \frac{1}{q_m K_L} + \frac{C_e}{q_m} \quad (11)$$

$$\ln q_e = \frac{1}{n} \ln C_e + \ln K_F \quad (12)$$

$$q_e = B \ln K_T + B \ln C_e \quad (13)$$

where  $C_e$  is the adsorbate concentration at equilibrium (mg L<sup>-1</sup>),  $q_e$  is the amount of adsorbate per unit of adsorbent (mg g<sup>-1</sup>),  $q_m$  is the maximum monolayer adsorption capacity of the adsorbent (mg g<sup>-1</sup>), and  $K_L$  represents the Langmuir adsorption constant (L mg<sup>-1</sup>). In addition,  $q_e$  is the amount of adsorbate adsorbed per unit mass of adsorbent (mg g<sup>-1</sup>),  $K_F$  is the Freundlich isotherm constant mg g<sup>-1</sup> (L mg<sup>-1</sup>)<sup>1/n</sup>,  $n$  is the heterogeneity factor, and  $B$  is the constant related to the heat of adsorption (L mg<sup>-1</sup>).

The plot of the isotherm models is represented in Fig. 17a–c, and the values are tabulated in Table 5. The correlation coefficient ( $R^2$ ) values were obtained as follows: Langmuir model is  $R^2 = 0.9903$ , Freundlich is  $R^2 = 0.1986$ , and Temkin is  $R^2 = 0.1448$ . Hence, the adsorption process is best fitted with the Langmuir adsorption model, indicating that the adsorption occurred by the formation of a monolayer of dye molecule on the adsorbent surface.

## 4. Conclusion

Cerium-doped copper zinc ferrite,  $\text{Ni}_{0.6}\text{Cu}_{0.4}\text{Ce}_x\text{Fe}_{2-x}\text{O}_4$  ( $x = 0.0, 0.5, 1.0, 1.5$ ), has been successfully synthesized by the co-precipitation method. The FTIR and XRD analyses confirmed the successful formation of cerium-doped ferrite with relatively smaller crystallite size, while the morphological analysis has shown that the particles have agglomeration. The synthesized catalyst has been successfully utilized in the degradation of

congo red dye *via* photocatalytic process, varying doses, concentrations, and pH. The catalyst exhibited the highest efficiency of  $\sim 91\%$  (when  $x = 1.5$ ) in degrading CR at a dose of 60 mg dose in a 40 ppm CR solution at pH 6.5. Batch studies were conducted to evaluate the influence of light on the degradation efficiency, revealing a higher percentage of degradation under light compared to a dark system. The radical scavenging assay was performed to understand the degradation pathway and identified  $\text{h}^+$  as the primary reactive species responsible for this degradation. Moreover, the catalyst has potent recycling qualities and is not structurally altered when it is recycled. The kinetic studies showed that the system followed a pseudo-second-order kinetic model, thus corresponding to a chemisorption process. Furthermore, adsorption isotherm studies revealed that the Langmuir isotherm was most suitable for describing the system, outperforming the Freundlich and Temkin isotherms.

## Data availability

The data that support the findings of this study are available on request from the corresponding author. The data are not publicly available due to restrictions [e.g., their containing information that could compromise the privacy of research participants].

## Author contributions

Morsueda Akhter: validation, investigation, formal analysis, software, writing – original draft; Md. Khairul Amin: visualization, writing – review & editing; Palash Kumar Dhar: writing – review & editing; Shishir Kumar Dey: writing – review & editing; Sagar Kumar Dutta: conceptualization, methodology, visualization, software, supervision.

## Conflicts of interest

The authors declare that they have no known competing financial interests or personal relationships that could have appeared to influence the work reported in this paper.

## Acknowledgements

The authors are grateful to Chemistry Discipline, Khulna University, Khulna-9208 for providing the necessary laboratory facilities.



## References

1 A. Soufi, H. Hajjaoui, R. Elmoubarek, M. Abdennouri, S. Qourzal and N. Barka, *Appl. Surf. Sci. Adv.*, 2022, **9**, 100251.

2 K. K. Kefeni and B. B. Mamba, *Sustainable Mater. Technol.*, 2020, **23**, e00140.

3 E. N. Zare, S. Iftekhar, Y. Park, J. Joseph, V. Srivastava, M. A. Khan, P. Makvandi, M. Sillanpaa and R. S. Varma, *Chemosphere*, 2021, **280**, 130907.

4 H. Liu, C. Wang and G. Wang, *Chem.-Asian J.*, 2020, **15**, 3239–3253.

5 Y. Yang, N. Ali, A. Khan, S. Khan, S. Khan, H. Khan, S. Xiaoqi, W. Ahmad, S. Uddin, N. Ali and M. Bilal, *Int. J. Biol. Macromol.*, 2021, **167**, 169–181.

6 B. Sharma, S. Tiwari, N. Bisht and L. Tewari, *Ind. Crops Prod.*, 2021, **170**, 113755.

7 K. Naseem, Z. H. Farooqi, R. Begum and A. Irfan, *J. Cleaner Prod.*, 2018, **187**, 296–307.

8 A. I. Borhan, P. Samoila, V. Hulea, A. R. Iordan and M. N. Palamaru, *J. Photochem. Photobiol. A*, 2014, **279**, 17–23.

9 T. de Oliveira Guidolin, N. M. Possolli, M. B. Polla, T. B. Wermuth, T. Franco de Oliveira, S. Eller, O. R. Klegues Montedo, S. Arcaro and M. A. P. Cechinel, *J. Cleaner Prod.*, 2021, **318**, 128556.

10 M. Haneef, I. H. Gul, M. Hussain and I. Hassan, *J. Supercond. Novel Magn.*, 2021, **34**, 1467–1476.

11 E. Z. Hegazy, S. A. Kosa, I. H. Abd Elmaksod and J. T. Mojammami, *Ceram. Int.*, 2019, **45**, 7318–7327.

12 Z. K. Heiba, M. Bakr Mohamed, L. Arda and N. Dogan, *J. Magn. Magn. Mater.*, 2015, **391**, 195–202.

13 P. Zhang, B. Yu and L. Zhang, *Sci. China, Ser. B: Chem.*, 2009, **52**, 101–108.

14 P. Samoila, C. Cojocaru, L. Sacarescu, P. Pascariu, A. Domocos and A. Rotaru, *Appl. Catal., B*, 2017, **202**, 21–32.

15 K. Tanbir, M. Prasad, G. Rakesh, K. Singh, M. Kar and S. Mukherjee, *J. Mater. Sci.: Mater. Electron.*, 2020, **31**, 435–443.

16 S. Jauhar, S. Singhal and M. Dhiman, *Appl. Catal., A*, 2014, **486**, 210–218.

17 D. D. Andhare, S. R. Patade, J. S. Kounsalye and K. M. Jadhav, *Phys. B Condens. Matter*, 2020, **583**, 412051.

18 M. A. Camacho-González, M. Quezada-Cruz, G. I. Cerón-Montes, M. F. Ramírez-Ayala, L. E. Hernández-Cruz and A. Garrido-Hernández, *Mater. Chem. Phys.*, 2019, **236**, 121808.

19 A. Hakeem, T. Alshahrani, G. Muhammad, M. H. Alhossainy, A. Laref, A. Rauf, I. Ali, H. Muhammad, T. Farid, T. Ghrib, S. Rabia and R. Yasmin, *J. Mater. Res. Technol.*, 2020, **11**, 158–169.

20 Y. Peng, C. Xia, M. Cui, Z. Yao and X. Yi, *Ultrason. Sonochem.*, 2021, **71**, 105369.

21 F. A. Hezam, N. O. Khalifa, O. Nur and M. A. Mustafa, *Mater. Chem. Phys.*, 2021, **257**, 123770.

22 M. Kamran and M. Anis-ur-Rehman, *J. Alloys Compd.*, 2020, **822**, 153583.

23 M. V. Limaye, S. B. Singh, S. K. Date, D. Kothari, V. R. Reddy, A. Gupta, V. Sathe, R. J. Choudhary and S. K. Kulkarni, *J. Phys. Chem. B*, 2009, **113**, 9070–9076.

24 K. Maaz, S. Karim, A. Mashiatullah, J. Liu, M. D. Hou, Y. M. Sun, J. L. Duan, H. J. Yao, D. Mo and Y. F. Chen, *Phys. B Condens. Matter*, 2009, **404**, 3947–3951.

25 S. Manouchehri, S. T. Mohammadi Benehi and M. H. Yousefi, *J. Supercond. Novel Magn.*, 2016, **29**, 2179–2188.

26 A. H. Zyoud, A. Zubi, S. H. Zyoud, M. H. Hilal, S. Zyoud, N. Qamhieh, A. R. Hajamohideen and H. S. Hilal, *Appl. Clay Sci.*, 2019, **182**, 105294.

27 D. Chahar, S. Taneja, S. Bisht, S. Kesarwani, P. Thakur, A. Thakur and P. B. Sharma, *J. Alloys Compd.*, 2021, **851**, 156878.

28 N. Abbas, N. Rubab, K. H. Kim, R. Chaudhry, S. Manzoor, N. Raza, M. Tariq, J. Lee and S. Manzoor, *J. Colloid Interface Sci.*, 2021, **594**, 902–913.

29 M. N. Alshabanat and M. M. Al-Anazy, *J. Chem.*, 2018, **1**, 9651850.

30 R. Behura, R. Sakthivel and N. Das, *Powder Technol.*, 2021, **386**, 519–527.

31 N. Elamin, A. Modwi, M. A. B. Aissa, K. K. Taha, O. K. Al-Duaj and T. A. Yousef, *J. Mater. Sci.: Mater. Electron.*, 2021, **32**, 2234–2248.

32 S. Qamar, M. N. Akhtar, K. M. Batoo and E. H. Raslan, *Ceram. Int.*, 2020, **46**, 14481–14487.

33 S. Jauhar and S. Singhal, *Ceram. Int.*, 2014, **40**, 11845–11855.

34 R. Zakir, S. S. Iqbal, A. U. Rehman, S. Nosheen, T. S. Ahmad, N. Ehsan and F. Inam, *Ceram. Int.*, 2021, **47**, 28575–28583.

35 S. Anjum, T. Zeeshan, S. Waseem, I. Waseem and Z. Mustafa, *Appl. Phys. A: Mater. Sci. Process.*, 2022, **128**, 1–13.

36 B. Bhujun, M. T. T. Tan and A. S. Shanmugam, *Results Phys.*, 2017, **7**, 345–353.

37 S. Debnath, K. Deb, B. Saha and R. Das, *J. Phys. Chem. Solids*, 2019, **134**, 105–114.

38 K. Hussain, N. Amin and M. I. Arshad, *Ceram. Int.*, 2021, **47**, 3401–3410.

39 E. Hema, A. Manikandan, P. Karthika, S. A. Antony and B. R. Venkatraman, *J. Supercond. Novel Magn.*, 2015, **28**, 2539–2552.

40 S. Kumar, S. Kumari, M. Kar, A. Singh, H. Pathak, J. P. Borah and L. Kumar, *J. Phys. Chem. Solids*, 2021, **151**, 109928.

41 J. Sarkar, S. Kalyan Roy, A. Laskar, D. Chattopadhyay and K. Acharya, *Mater. Lett.*, 2013, **92**, 313–316.

42 M. Rouchdi, H. Mamori, E. Salmani, B. Ait Syad, O. Mounkachi, R. Essajai, H. Ez-zahraouy, H. Chakchak, N. Hassanain, A. Benyoussef, A. El Kenz and A. Mzerd, *Appl. Phys. A: Mater. Sci. Process.*, 2021, **127**, 1–14.

43 Y. Orooji, M. Ghanbari, O. Amiri and M. Salavati-Niasari, *J. Hazard. Mater.*, 2020, **389**, 122079.

44 N. Hosni, K. Zehani, T. Bartoli, L. Bessais and H. Maghraoui-meherzi, *J. Alloys Compd.*, 2017, **694**, 1295–1301.

45 E. Peng, X. Wei, T. S. Herng, U. Garbe, D. Yu and J. Ding, *RSC Adv.*, 2017, **7**, 27128–27138.



46 N. Ali, A. Said, F. Ali, F. Raziq, Z. Ali, M. Bilal, L. Reinert, T. Begum and H. M. N. Iqbal, *Water, Air, Soil Pollut.*, 2020, **231**, 1–16.

47 A. Zamani, M. Seyed, S. Alireza, M. Mohammad and Y. Nazanin, *Int. J. Ind. Chem.*, 2020, **11**, 205–216.

48 K. M. Reza, A. Kurny and F. Gulshan, *Appl. Water Sci.*, 2017, **7**, 1569–1578.

49 Z. U. H. Khan, A. Khan, N. S. Shah, I. U. Din, M. A. Salam, J. Iqbal, N. Muhammad, M. Imran, M. Ali, M. Sayed and M. A. Gohar, *Surf. Interfaces*, 2021, **23**, 100944.

50 W. Shi, X. Liu, T. Zhang, Q. Wang and L. Zhang, *RSC Adv.*, 2015, **5**, 51027–51034.

51 S. A. Bhat, F. Zafar, A. H. Mondal, A. Kareem, A. U. Mirza, S. Khan, A. Mohammad, Q. M. R. Haq and N. Nishat, *J. Iran. Chem. Soc.*, 2020, **17**, 215–227.

52 A. Singh, A. Ahmed, A. Sharma, C. Sharma, S. Paul, A. Khosla, V. Gupta and S. Arya, *Phys. B Condens. Matter*, 2021, **616**, 413121.

53 S. Swathi, R. Yuvakkumar, P. S. Kumar, G. Ravi and D. Velauthapillai, *Chemosphere*, 2021, **281**, 130903.

54 P. Yadav, P. K. Surolia and D. Vaya, *Mater. Today: Proc.*, 2021, **43**, 2949–2953.

55 R. Jasrotia, N. Kumari, R. Kumar, M. Naushad, P. Dhiman and G. Sharma, *Earth Syst. Environ.*, 2021, **5**, 399–417.

56 C. Aoopngan, J. Nonkumwong, S. Phumying, W. Promjantuek, S. Maensiri, P. Noisa, S. Pinitsoontorn, S. Ananta and L. Srisombat, *ACS Appl. Nano Mater.*, 2019, **8**, 5329–5341.

57 C. Lei, M. Pi, P. Kuang, Y. Guo and F. Zhang, *J. Colloid Interface Sci.*, 2017, **496**, 158–166.

